ELSEVIER

Journal of Nuclear Materials 251 (1997) 49–60

journal of nuclear materials

Primary damage formation in bcc iron

R.E. Stoller [a,*], G.R. Odette [b], B.D. Wirth [b]

[a] *Metals and Ceramics Division, Oak Ridge National Laboratory, Oak Ridge, TN 37831-6376, USA*
[b] *Department of Mechanical and Environmental Engineering, University of California, Santa Barbara, CA 93106, USA*

Abstract

Primary defect formation in bcc iron has been extensively investigated using the methods of molecular dynamics (MD) and Monte Carlo (MC) simulation. This research has employed a modified version of the Finnis–Sinclair interatomic potential. MD was used in the simulation of displacement cascades with energies up to 40 keV and to examine the migration of the interstitial clusters that were observed to form in the cascade simulations. Interstitial cluster binding energies and the stable cluster configurations were determined by structural relaxation and energy minimization using a MC method with simulated annealing. Clusters containing up to 19 interstitials were examined. Taken together with the previous work, these new simulations provide a reasonably complete description of primary defect formation in iron. The results of the displacement cascade simulations have been used to characterize the energy and temperature dependence of primary defect formation in terms of two parameters: (1) the number of surviving point defects and (2) the fraction of the surviving defects that are contained in clusters. The number of surviving point defects is expressed as a fraction of the atomic displacements calculated using the secondary displacement model of Norgett–Robinson–Torrens (NRT). Although the results of the high energy simulations are generally consistent with those obtained at lower energies, two notable exceptions were observed. The first is that extensive subcascade formation at 40 keV leads to a higher defect survival fraction than would be predicted from extrapolation of the results obtained for energies up to 20 keV. The stable defect fraction obtained from the MD simulations is a smoothly decreasing function up to 20 keV. Subcascade formation leads to a slight increase in this ratio at 40 keV, where the value is about the same as at 10 keV. Secondly, the potential for a significant level of in-cascade vacancy clustering was observed. Previous cascade studies employing this potential have reported extensive interstitial clustering, but little evidence of vacancy clustering. Interstitial clusters were found to be strongly bound, with binding energies in excess of 1 eV. The larger clusters exhibited a complex, 3D structure and were composed of ⟨111⟩ crowdions. These clusters were observed to migrate by collective ⟨111⟩ translations with an activation energy on the order of 0.1 eV. © 1997 Elsevier Science B.V.

1. Introduction

Although the time scale required for radiation-induced mechanical property changes to occur can range from weeks to years, the primary damage event leading to these changes lasts only about 10^{-11} s. A similar comparison can be made between the size scales of this primary damage event and the components that are affected. For example, the pressure vessel in a nuclear power plant is several meters in height and diameter while the primary damage event that leads to the embrittlement of the ferritic steel is contained within 10^{-8} m. This primary damage event is the displacement cascade that occurs when a lattice atom is displaced by an energetic particle. In the case of materials used in nuclear power systems, the particle initiating the displacement cascade is typically a neutron with up to 10 MeV of kinetic energy. Since the spatial and time resolution required to study the cascade evolution directly is not available by any experimental means, computer simulation provides the best means of investigating these events. Although the use of molecular dynamics (MD) as a tool for simulating displacement cascades was pioneered by Vineyard and co-workers at the Brookhaven National Laboratory in the 1960s [1], it is only

* Corresponding author. Tel.: +1-423 576 7886; fax: +1-423 574 0641; e-mail: rkn@ornl.gov.

PII S0022-3115(97)00256-0

with the recent increase in computing power offered by modern machines that the method could be applied to systems large enough to explore the energy range of interest to reactor materials [2–12].

The embedded-atom type interatomic potential developed by Finnis and Sinclair [13] has been used in several molecular dynamics studies of displacement cascade evolution and point defect behavior in iron [2–7,13–15]. The predicted properties of stable point defects and small point defect clusters were initially investigated by Harder and Bacon [15], and their work has been extended by Wirth and Odette [14]. This latter work employed a version of the potential that had been modified by Calder and Bacon [5] to permit the potential to be used for high-energy displacement cascade simulations. The modification was necessary in order to obtain a realistic simulation of high-energy elastic collisions because the potential was too 'soft' at very short interatomic separations. Following the modification, the potential was shown to give reasonable agreement with the expected pressure–volume relationship for the perfect crystal and for the atomic displacement threshold in both the ⟨100⟩ and ⟨110⟩ directions [5,7].

The previous research conducted by the authors and their collaborators has been extended in several areas and, together with the previous work, the results presented here provide a reasonably complete description of primary defect formation in iron. This new work includes cascade simulation energies as high as 40 keV, demonstrating the effect of subcascade formation. A more detailed analysis of both the 40 keV cascades and some of those conducted earlier at 10 and 20 keV provides new evidence of vacancy clustering in iron. In order to answer some questions about the way in which these MD simulations are normally conducted, the effects of primary knock-on (PKA) direction and lattice temperature due to cascade heating have been investigated. The relative stability of the alternate self-interstitial configurations has been examined, and the mechanism of interstitial migration has been determined. In addition, the stability and structure of interstitial clusters have been determined for sizes up to a 19-interstitial cluster and the mobility of these clusters has been examined.

2. Simulation models and methods

The modified version of the Finnis–Sinclair interatomic potential for iron mentioned above was used in this work [5,7,13]. This potential was implemented in the vectorized MOLDY code of Finnis [16], a code used by many researchers in this subject area. MOLDY uses the link cell method to generate neighbor tables for interactions between atoms and a variable timestep, which is determined by the energy and interaction of the atoms. Constant pressure, periodic boundary conditions were employed for all the simulations discussed here. The size of the atom block was increased for higher energies and temperatures so that the cascade was retained within the block and no artificial overlap of the cascade regions occurred. The maximum block size for each simulation energy is shown in Table 1. Most of these calculations were carried out on modern, high-speed workstations, where two to three weeks of cpu time is required to complete a typical 40 keV cascade.

The boundary atoms were not damped to extract heat or attenuate the outgoing pressure wave. This causes the atom block to heat up and extends the lifetime of the thermal spike. However, the temperature dependence of the surviving defect fraction and the defect clustering fraction have been shown to be weak [3], indicating that the effect of not having a surface heat sink should be small. This inference is supported by some of the work discussed below and is consistent with a more detailed examination of the effects of cascade temperature that was conducted by Gao et al. [17]. Additional details on the method followed and the limitations imposed thereby can be found in Refs. [2–5]. Refs. [8,18] also provide useful background information on the use of MD for displacement cascade simulations.

Before initiating a cascade, an atom block of the desired size was thermally equilibrated at the desired temperature for approximately 10 ps to permit phonon waves to be established. This atom block was then saved and used as the starting point for the subsequent cascade simulations. Cascade simulations were initiated by giving one of the atoms a defined amount of kinetic energy in a specified direction. Variability was introduced by either further equi-

Table 1
Typical MD cascade parameters and required atom block sizes

Neutron energy (MeV)	Average PKA energy (keV)	Corresponding $T_{dam} \cong E_{MD}$ (keV)	NRT displacements	Atoms in simulation
0.0034	0.116	0.1	1	3456
0.0058	0.236	0.2	2	6750
0.014	0.605	0.5	5	6750
0.036	1.24	1.0	10	54000
0.074	2.54	2.0	20	54000
0.19	6.6	5.0	50	128000
0.40	13.7	10.0	100	250000
0.83	28.8	20.0	200	250000
1.8	61.3	40.0	400	1024000

libration of the starting block, choosing a different primary knockon atom, or a combination of both. The progress of each cascade was monitored graphically to determine when the event was completed. Depending on the PKA energy and the irradiation temperature, the total simulation time required varies from about 5 to 25 ps. The final state of the atom block was then examined to count the number and distribution of the remaining point defects. A graphics visualization program, '*atomtv*', developed and distributed by Rudy Ziegler at the University of Toronto was particularly useful in the analysis of the cascade residue. This program can be obtained on the world-wide web at ftp://ftp.hprc.utoronto.ca/pub/atomtv. At least six cascades were averaged at each condition to insure that the results were statistically significant.

The results of the displacement cascade simulations are described primarily by two parameters: (1) the number of surviving point defects and (2) the fraction of the surviving defects contained in clusters. These clusters are formed directly within the displacement cascade and are visible immediately after the cascade begins to cool at about 1 ps. The number of surviving point defects is also expressed as a fraction of the atomic displacements calculated using the secondary displacement model of Norgett–Robinson–Torrens (NRT) [19] [1]. The NRT model gives the total number of displaced atoms produced by a PKA with kinetic energy E_{PKA} as

$$\nu_{NRT} = 0.8\frac{T_{dam}(E_{PKA})}{2E_d}, \quad (1)$$

where E_d is an average displacement threshold energy and the damage energy, T_{dam}, is a function of E_{PKA}. The recommended value of E_d for iron is 40 eV [21]. The damage energy is the amount of the initial PKA energy available to cause atomic displacements. Kinetic energy lost to electronic excitation is responsible for the difference between E_{PKA} and T_{dam}. The damage energy can be calculated using a numerical approximation to the theory of Lindhard et al. [19–21] and the ratio T_{dam}/E_{PKA} varies from 0.86 for a damage energy of 100 eV to 0.65 at 40 keV. Since the MD cascade simulations do not account for electronic losses, the cascade simulation energy E_{MD} is approximately equivalent to T_{dam}.

The dynamics of point defect and self-interstitial cluster migration were also investigated by isothermal–isobaric MD simulations using the MOLDY code. Calculations of the self-interstitial and self-interstitial cluster formation energies and structural characteristics were performed by a simulated annealing method based on isothermal–isobaric Metropolis Monte Carlo (MC) simulation in conjunction with steepest-descent quenching [22]. The MC simulations employed a semi-empirical description of the interatomic potential by Finnis and Sinclair [13]. The MD simulations of point defect and cluster migration were performed over the temperature range of 100 to 1000 K in simulation super cells with sizes ranging from $2000 + N$ to $8192 + N$ where N is the number of self-interstitial atoms in the super cell.

To investigate the structure and energetics of self-interstitial clusters a relaxation schedule was employed consisting of 12 cooling stages at temperatures of 1050, 900, 800, 600, 400, 250, 150, 50, 10, 1, 0.1 and 0.01 K for each cluster size. At each cooling stage, the structure was equilibrated thermally by MC simulation at zero pressure. The resulting equilibrated configuration was mapped onto its corresponding local minimum-energy configuration by steepest-descent quenching. This quenched configuration provided the initial atomic configuration for repeating the procedure at the next cooling stage. More details on the MC method can be obtained in Refs. [14,22]. The initial configuration of the first cooling stage for a cluster of N self-interstitial atoms consisted of N randomly oriented interstitial dumbbells about N neighboring lattice sites in a region around the geometrical center of the supercell. To ensure that the above relaxation procedure gave the ground-state configuration of the cluster, the procedure was repeated for several cluster sizes (N). These calculations were started with different higher-symmetry initial configurations, such as planar configurations with all interstitial dumbbells oriented in the same direction and lying on the same plane. Different supercell sizes were used to ensure that strain interactions of the cluster due to the periodic boundary conditions were negligible.

3. Results and discussion

3.1. Cascade simulations

Four aspects of the cascade simulations will be discussed. The first is the effect of PKA direction. The results of 1 keV cascades initiated in the ⟨100⟩, ⟨110⟩, and ⟨111⟩ directions are compared with those initiated using the typical high index ⟨135⟩ direction. Next, the effect of lattice temperature will be examined by comparing the results obtained when the same 20 keV cascade was run for 200 ps under two different sets of conditions that led to final temperatures of 54 and 135 K. Then, the impact of subcascade formation at high cascade energies will be illustrated by comparing new results at 40 keV with those obtained for cascades up to 20 keV. Finally, the issue of vacancy clustering in the iron cascades will be addressed.

3.1.1. Dependence of defect survival on PKA direction

A high index direction such as the ⟨135⟩ is typically chosen in cascade simulations to avoid lattice effects such as channeling or directions with particularly low or high

[1] See also Ref. [20].

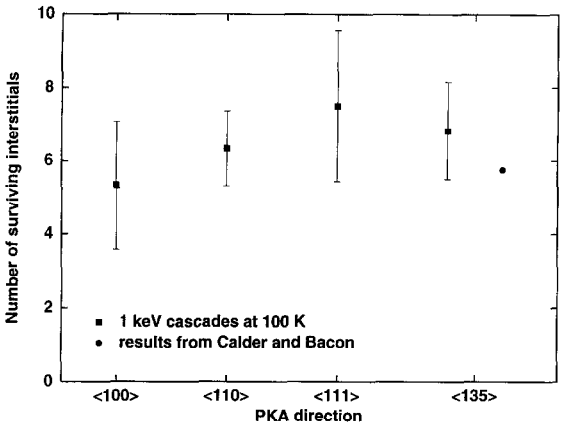

Fig. 1. Dependence of point defect survival on PKA direction in 1 keV cascades at 100 K; averages and standard deviations from six cascades are shown.

displacement thresholds. Such a direction is implicitly assumed to yield results that are representative of some appropriate average behavior. In order to examine this assumption, a series of 1 keV cascades were run in a block of 54,000 atoms that had been equilibrated at 100 K. Six different cascades were initiated in each of the ⟨100⟩, ⟨110⟩, ⟨111⟩ and ⟨135⟩ directions. The displacement threshold is lowest for the ⟨100⟩ direction, highest for the ⟨111⟩ direction and intermediate in the ⟨110⟩ direction [7]. These results can also be compared with the averages obtained from four similar 1 keV, 100 K, ⟨135⟩ cascades previously conducted in a 16,000 atom block by Calder and Bacon [5].

The final number of surviving interstitials is shown in Fig. 1 for each PKA direction. The data point is the average obtained from the six cascades and the error bars represent one standard deviation. The results of Calder and Bacon are shown without an error bar. Although the standard deviation is rather large for only six cascades, a systematic trend is observed; fewer stable defects are produced in the more open lattice directions. This trend is opposite to that of the displacement threshold, i.e., fewer net defects are produced in the directions with lower displacement thresholds [5,7]. Additional results are given in Table 2, where the number of defects at the time of peak disorder and the interstitial clustering fraction are also listed. No statistically significant trend can be determined in these latter two quantities.

It would not be practical to conduct the very large number of cascades in the range of PKA directions that would be required to determine the directionally-averaged cascade behavior. However, the values listed in Table 1 and shown in Fig. 1 indicate that the results obtained from the ⟨135⟩ cascades lie between the extremes of the values obtained for cascades in three low index directions. These three directions cover the range of very low to very high displacement thresholds, and open to close-packed directions. Although the average interstitial clustering fractions shown in Table 2 do not appear to simply correlate with PKA direction, the average value for the ⟨135⟩ cascades is within the range calculated for the low index directions. Overall, these results support the view that the ⟨135⟩ cascades should provide a reasonable representation of average behavior.

3.1.2. *Impact of lattice temperature loss*

As mentioned above, the boundary atoms in the cascade simulations were not damped. Some heating of the lattice is therefore observed when the energy of the PKA is injected into the lattice. Gao et al. have examined the effect of lattice heating using a hybrid model in which the MD block is embedded within a larger, continuum ('thermal') block [17]. Their thermal block acts as a heat sink at the boundary of the MD block. Although an influence of thermal damping was observed, the overall effect was rather small. However, another factor that can affect the lattice temperature in MD cascade simulations is the finite numerical accuracy obtained in the numerical integration of the equations of motion. An upper limit to the variable time step is specified as an input parameter in MOLDY. Larger timesteps permit the calculations to be completed in less real time, but reduced accuracy is obtained in the integration. This can lead to a significant artificial cooling of the cascade, particularly in long running simulations.

An example of the influence of finite precision is shown in Fig. 2, where the atom block temperature is plotted for a 20 keV cascade that was initiated at 100 K and run for 200 ps. In this simulation, the number of residual point defects had stabilized by about 20 ps. The simulation was continued for another 180 ps to investigate the restructuring of the cascade residue due to the migration of interstitials and small interstitial clusters. Note that the cascade temperature was still about 370 K at 20 ps, but had dropped to 54 K at 200 ps. While the number of surviving defects did not appear to be changing, this

Table 2
Average defect formation parameters and standard deviations (σ) from sets of six 1 keV cascades at 100 K in a block of 54000 atoms

PKA direction	Surviving defects	$\pm\sigma$	Defects at peak	$\pm\sigma$	Clustered interstitial fraction
⟨100⟩	5.33	1.75	230.0	7.21	0.34
⟨110⟩	6.33	1.03	222.8	24.3	0.29
⟨111⟩	7.50	2.07	220.7	29.6	0.40
⟨135⟩	6.83	1.33	219.7	23.9	0.37
⟨135⟩[a]	5.75	–	–	–	0.39

[a]Average values from four cascades in 16000 atom block by Calder and Bacon [5], standard deviation not available.

temperature drop could have influenced the amount of interstitial clustering that occurred. In order to investigate this possibility, the simulation was restarted from an intermediate file containing the necessary information on the state of the atom block when the temperature was 175 K. The maximum time step was reduced from 7×10^{-15} to 5×10^{-15} s at this point. This is illustrated in Fig. 2 by the arrow at a time of 83 ps.

As shown in Fig. 2, the reduction in the timestep reduced the rate at which energy was lost from the system. The temperature at 200 ps obtained with the smaller timestep was 133 K. As expected, the total number of point defects at 200 ps was the same with either timestep; 48 Frenkel pair remained. The fraction of clustered interstitials also remained the same; 34 of the 48 remaining interstitials were in clusters in both cases. Similarly, the vacancy clustering fraction was not changed. Only in the interstitial cluster size distribution was a small change observed. For the original case with a maximum timestep size of 7×10^{-15} s, there were 14 interstitials, seven di-interstitials, two tri-interstitials, one 5-interstitial cluster and one 9-interstitial cluster. The higher temperature maintained by the smaller timestep permitted the coalescence of two di-interstitials into a single tetra-interstitial.

This simple comparison involving a single cascade obviously can not provide a definitive demonstration that the effects of lattice heating or finite precision do not influence the results of the MD cascade simulations. However, this comparison is consistent with earlier work in which it was shown that both the point defect survival fraction and the interstitial clustering fraction were only weakly dependent on temperature in the range of 100 to 900 K [3], and the more detailed examination of cascade temperature effects reported in Ref. [17].

3.1.3. Impact of subcascade formation on defect formation parameters

The maximum energy reached in MD cascade simulations previously reported in iron is 20 keV [3,6]. Six 40

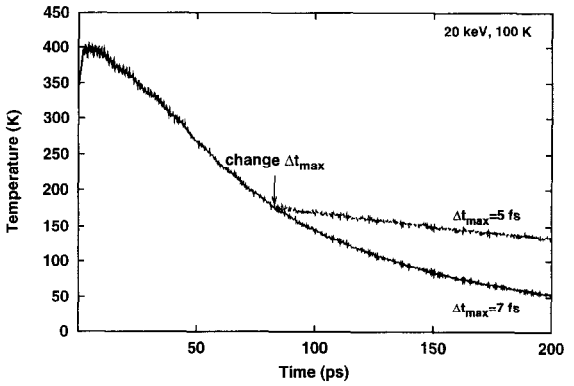

Fig. 2. Example of energy loss due to finite accuracy in numerical integration, maximum timestep was reduced from 7×10^{-15} to 5×10^{-15} s at the time indicated.

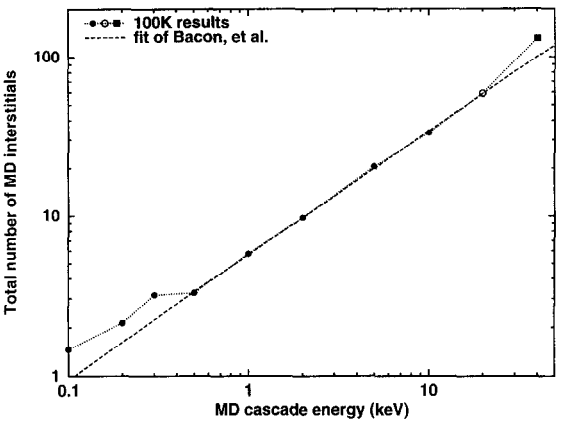

Fig. 3. Average number of surviving interstitials in cascades at 100 K and power-law fit obtained by Bacon et al. [11].

keV cascades at 100 K have now been completed. This MD cascade energy corresponds to a PKA energy of 61 keV, which is the average iron PKA energy from an elastic collision with a 1.8 MeV neutron. Thus, these new simulations have reached well into the energy range of fast neutrons obtained from fission. For example, 91% of the neutrons in the peripheral target position in the high flux isotope reactor at the Oak Ridge National Laboratory have energies below 1.8 MeV.

Based on the results of cascades in iron up to 10 keV and at 100 K, Bacon, et al. found that the total number of surviving point defects, N_D, could be described by a simple power law [11]:

$$N_D = 5.67 E_{MD}^{0.779}, \tag{2}$$

where the cascade energy, E_{MD} is given in keV. Eq. (2) is plotted in Fig. 3, along with the average number of surviving interstitials at several energies. The deviation from the line at low energies can be explained by the fact that well developed displacement cascades are not observed at these energies. Later, ten 20 keV cascades were completed [3,6] and the average value of N_D at this energy was found to lie on the same line as shown in Fig. 3.

However, there is no clear physical explanation for the sublinear energy dependence in Eq. (2); an exponent of 1.0 is predicted by the NRT model in Eq. (1). When the results of the six 40 keV cascades were averaged, N_D was found to lie well above the extrapolated power-law curve. This new data point is also shown in Fig. 3. Although there are insufficient data to establish a new trend, it is interesting to note that the slope between 20 and 40 keV is nearly 1.0. These same results are replotted in Fig. 4 in which the number of surviving interstitials is divided by the NRT displacements at each energy. The rapid drop in this MD defect survival ratio at low energies is well known. This effect is due to greater incascade recombination of vacancies and interstitials as the defect density in the cascade increases at higher energies. Just as the 40 keV data point

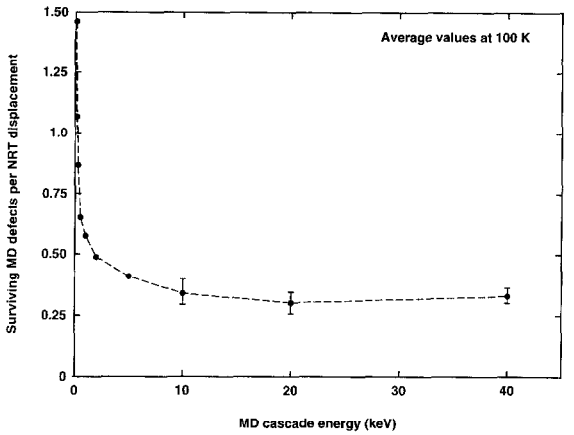

Fig. 4. Ratio of surviving MD interstitials or vacancies at 100 K to the number of displacements obtained from the NRT displacement model [19–21].

that fell above the power law curve in Fig. 3, the surviving defect fraction shows a slight increase as the cascade energy increases from 20 to 40 keV.

Based on the standard deviations of the averages shown in Fig. 4 at 10, 20 and 40 keV, it appears that this increase is statistically significant. The explanation for this behavior is shown in Fig. 5, where representative cascades at 10, 20 and 40 keV have been superimposed in a single atom block for purposes of comparison. Each cascade is shown near the time of peak disorder and only the interstitials are included for simplicity. The increasing tendency toward subcascade formation as the cascade energy increases is clearly illustrated. In the case of the 40 keV cascade, each of the well-separated subcascades is similar to a single cascade that would be obtained at a lower energy. Thus the average defect survival fraction at 40 keV lies between the values obtained at 10 and 20 keV. This result provides the most dramatic evidence of the impact of subcascade formation that has been observed at this time.

The incascade interstitial clustering fraction at 100 K is shown in Fig. 6 for energies out to 40 keV. The relative sensitivity of the interstitial clustering fraction is similar to that of the defect survival fraction, but energy dependence is reversed. Higher clustering fractions are obtained from higher energy cascades and an apparent saturation value of

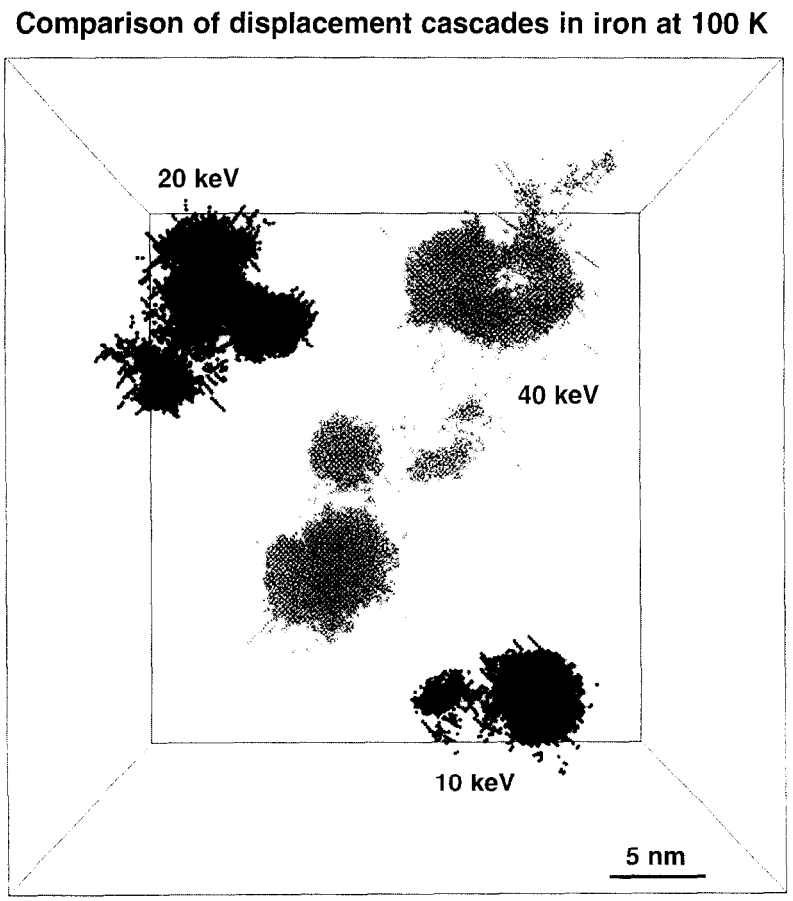

Fig. 5. Illustration of increasing subcascade formation at 100 K with increasing cascade energy; 10, 20 and 40 keV cascades are shown.

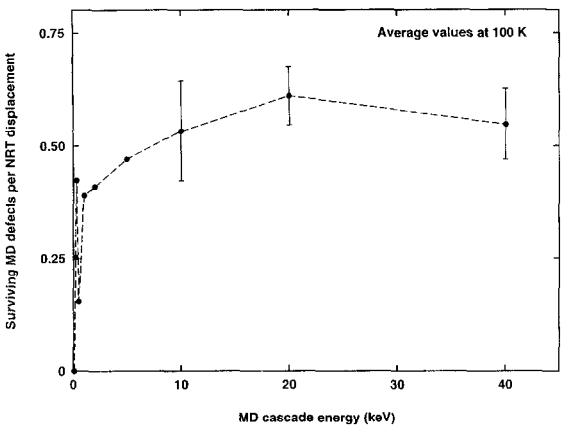

Fig. 6. Ratio of interstitials in clusters to total surviving MD interstitials at 100 K, spacing in units of lattice nearest neighbor (nn) distance.

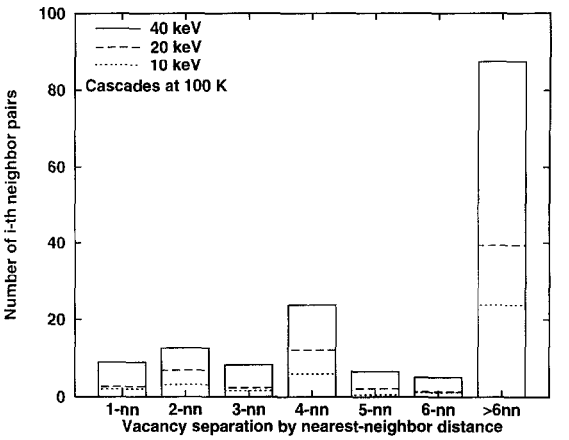

Fig. 7. Spatial correlation of all vacancies in 10, 20 and 40 keV cascades at 100 K.

about 0.55 is observed above 10 keV. As shown by the standard deviations in Fig. 6 at the highest three energies, the scatter in the clustering results is much greater than for defect survival. Therefore, it is not possible to determine if the decrease in the clustering fraction observed when the cascade energy increases from 20 to 40 keV represents a significant change.

3.1.4. Evidence of vacancy clustering

Previous analysis of the results of MD cascade simulations in iron using the Finnis–Sinclair potential have indicated that the amount of incascade vacancy clustering is relatively small [3–6]. Although more vacancy clustering was expected as the cascade energy increased, both the 20 and 40 keV cascades indicated that the vacancy clustering fraction remained less than 10%. These low vacancy clustering fractions were calculated using the same restrictive definition that had been applied to interstitial clustering, viz. that two defects had to be within the nearest neighbor lattice spacing to be considered clustered. Since interstitials are quite mobile in cascade simulations conducted at temperatures of 100 K and greater, some of the interstitial clusters observed are formed as single defects encounter one another in times less than 5 to 10 ps. However, vacancies are essentially immobile during the time span of these MD simulations ($\leq$ 200 ps). In order to estimate the potential for vacancy clustering over longer times, the 10, 20 and 40 keV cascades were reanalyzed to see if the vacancy locations were correlated at distances longer than the nearest neighbor distance.

The result of the vacancy analysis is shown in Fig. 7, where the number of vacancy–vacancy pairs at a given separation distance is plotted for all of the residual vacancies obtained from the cascades. The distance scale is in units of the nearest-neighbor lattice distance. The peaks in the histogram provide evidence of vacancy–vacancy correlation for all three energies out to the 4th nearest neighbor position. This spatial correlation can be considered as a measure of the potential for vacancy clustering to occur over the somewhat longer times required to permit a few vacancy jumps. The kinetics of such potential vacancy clustering can not be investigated by MD. Cascade annealing by Monte Carlo simulation is currently being applied to examine this behavior.

The average percentages of interstitials and vacancies in clusters at the end of the cascade period are compared in Fig. 8. Four values are shown for the vacancy cluster percentage at the highest three energies, reflecting four different clustering criteria. If vacancies separated by distances as large as the fourth nearest neighbor distance can be considered 'clustered,' the fraction of vacancies in clusters begins to approach that of interstitials in clusters.

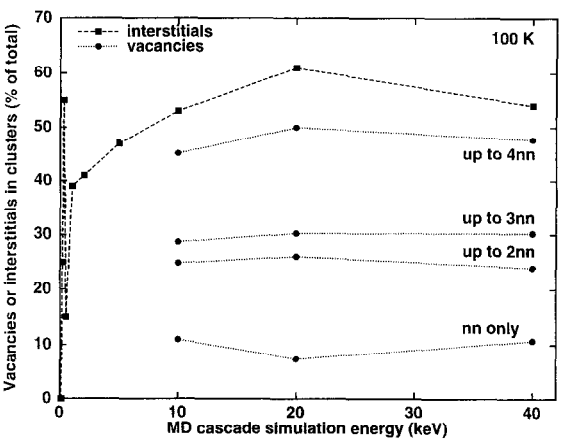

Fig. 8. Comparison of interstitial and vacancy clustering in cascades at 100 K. The three values for vacancy clustering reflect different clustering criteria: nearest neighbor (nn), second nearest neighbor (2nn), third nearest neighbor (3nn) and fourth nearest neighbor (4nn).

Table 3
Relaxed structure and formation properties of point-defects in α-iron. Relaxed self-interstitial atomic positions given in units of the lattice parameter, a_0, formation energy and formation volume given in units of atomic volume, Ω. The fully relaxed formation energy in units of eV and volume of the vacancy are given for comparison

Defect type	Atomic positions (a_0)	Formation energy (eV)	Formation volume (Ω)
⟨110⟩ dumbbell	(0.245, 0.245, 0.5) (0.755, 0.755, 0.5)	4.76	1.43
⟨111⟩ dumbbell	(0.291, 0.291, 0.291) (0.709, 0.709, 0.709)	4.87	1.74
⟨111⟩ crowdion	(0.331, 0.331, 0.331) (0.749, 0.749, 0.749) (1.167, 1.167, 1.167)	4.91	1.77
Vacancy	–	1.83	0.93

The amount of incascade clustering is important since these clusters provide easy nucleation sites for the growth of larger defects. This can reduce the irradiation dose required to induce microstructural evolution and the mechanical property changes which follow.

3.2. Interstitial cluster analysis

3.2.1. Structure of small self-interstitial clusters

The stable configuration for the single self-interstitial (SIA) in α-iron was found to be the ⟨110⟩ oriented split-interstitial dumbbell with a formation energy of 4.76 eV, in agreement with both previous atomistic simulations [5,15,23] and experiment [24]. Notably, two metastable configurations were found with respect to the stable configuration with a formation energy less than 0.15 eV above that of the ⟨110⟩ dumbbell. These two configurations are the ⟨111⟩ oriented split-interstitial dumbbell with a formation energy of 4.87 eV, and the crowdion configuration with a formation energy of 4.91 eV. The relaxed atomic positions and formation energies are given in Table 3, along with those of the vacancy for comparison. The crowdion is the saddle point for translation of the ⟨111⟩ dumbbell and can be considered to consist of three atoms sharing two lattice sites. The metastable configurations play a key role in the migration of the single interstitial, as discussed below.

While the stable configuration of a single self-interstitial in α-iron is the ⟨110⟩ oriented dumbbell, the stable configuration of clusters of two or more self-interstitials was found to consist of ⟨111⟩ oriented dumbbells, with an increasing number of dumbbells being replaced with crowdions as the cluster size (N) increases. Fig. 9 shows the stable configuration of clusters of size $N = 2$, 3 and 4. The stable two-member cluster, Fig. 9a, consists of two parallel ⟨111⟩ oriented SIA dumbbells which are centered about lattice sites which are third nearest neighbors. The stable three-member cluster, Fig. 9b, again consists of parallel aligned ⟨111⟩ SIA dumbbells. The stable four-member cluster, Fig. 9c, configuration consists of three dumbbells and one crowdion oriented along the [111] direction, two of which lie on one (110) plane and the other two on an adjacent (110) plane.

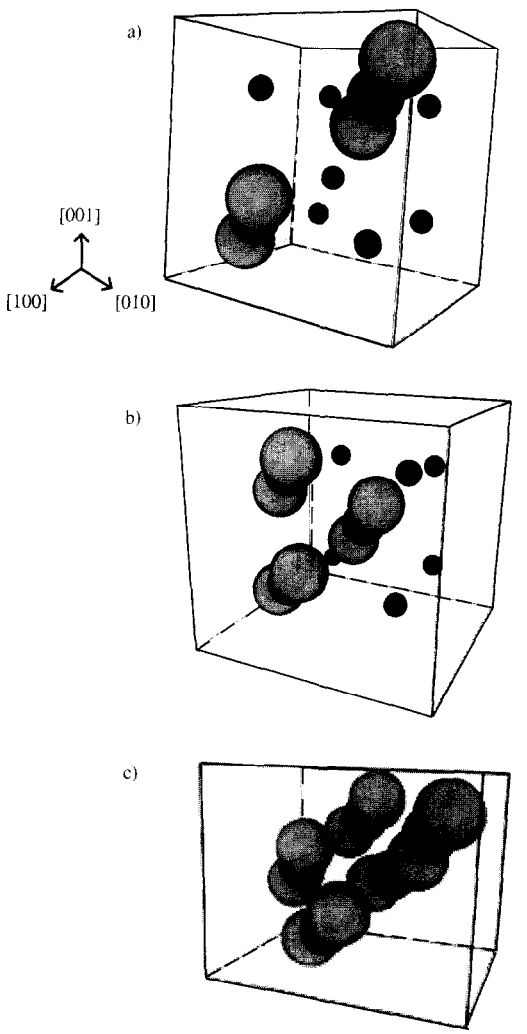

Fig. 9. Fully relaxed structure of self-interstitial clusters of size (a) $N = 2$, (b) $N = 3$ and (c) $N = 4$. Lattice atoms in their relaxed positions, vacant lattice sites and atoms displaced by more than 30% of the lattice parameter from their closest lattice site are denoted by small dark, large dark and large, light gray colored spheres, respectively. In the split-interstitial dumbbell configurations, one lattice site (dark) is shared by two atoms (light), while in the crowdion configurations two lattice sites (dark) are shared by three atoms (light).

The structural characteristics of the small self-interstitial clusters demonstrated in Fig. 9 are generic for self-interstitial clusters with sizes over the range $2 \leq N \leq 19$. The minimum energy cluster configurations consist of $\langle 111 \rangle$ dumbbells and/or crowdions that lie on one, two, or more adjacent $\{110\}$ planes and are oriented along $\langle 111 \rangle$ directions. Furthermore, the number of crowdions in the stable cluster configuration increases with the cluster size. The cluster morphology appears to be three-dimensional. The increasing number of crowdions in the clusters gives the impression of an extended defect configuration. For example, the stable configuration of a 19-member cluster consists of four $\langle 111 \rangle$ SIA dumbbells and $15\langle 111 \rangle$ crowdions situated on five adjacent $\{110\}$ planes. This fully relaxed structure is shown in Fig. 10.

The cluster formation energy E^F is plotted in Fig. 11 as a function of the cluster size N. The results of Fig. 11 show the strong binding energy of the interstitial clusters. The slope of the $E^F(N)$ curve is approximately 3 eV per self-interstitial atom compared with the formation energy of 4.76 eV of a single $\langle 110 \rangle$ self-interstitial dumbbell. The binding energy for the last interstitial atom to a cluster of size N is given by

$$E_N^B = \left(E_{N-1}^F + E_{\langle 110 \rangle}^F \right) - E_N^F. \quad (3)$$

The clusters are strongly bound, with binding energies in excess of 1 eV and which generally increase with increasing cluster size. The seven-member cluster has been found to be the most strongly bound cluster and the structure observed in the binding energy curve [14] suggests that there is a geometrically-preferred arrangement of interstitials in the clusters.

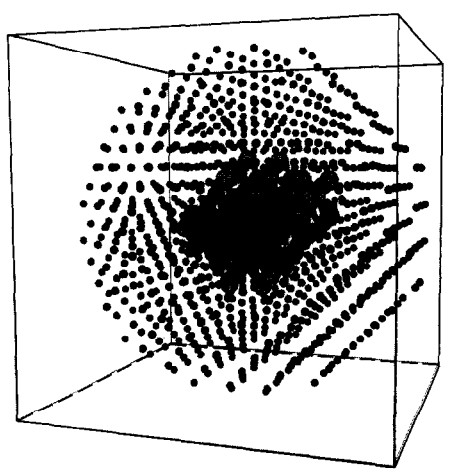

Fig. 10. Fully relaxed structure of self-interstitial cluster of size $N = 19$. Lattice atoms in their relaxed positions and atoms displaced by more than 30% of the lattice parameter from their closest lattice site are denoted by small dark spheres and large light gray spheres, respectively. The vacant lattice sites within the crowdions are visible in some cases as large dark spheres.

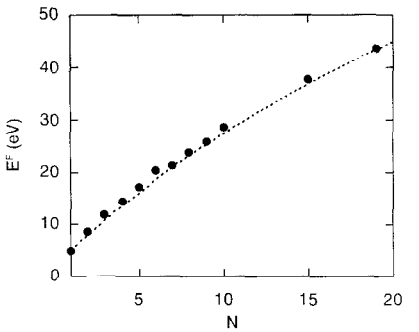

Fig. 11. Formation energy of self-interstitial clusters as a function of the cluster size N, where $N = 1$ corresponds to a single self-interstitial atom.

The three-dimensional morphology of the stable self-interstitial cluster structure is easily visualized as shown in Figs. 9 and 10. However, the possibility that the cluster has a dislocation loop morphology, as has been suggested in the literature [5,15,23] has also been examined, although it will not be discussed in detail in this review. An examination of the atomic stacking of a number of the self-interstitial clusters has not revealed a stacking fault. However, while the atomic stacking is consistent with a perfect extrinsic dislocation loop with a Burgers vector of $b = a/2\langle 111 \rangle$, the cluster configuration is more extended and three-dimensional than a perfect extrinsic dilocation platelet. Thus, we conclude that the morphology of these self-interstitial clusters is highly complex. The lowest energy configurations consist of $\langle 111 \rangle$ split-interstitial dumbbells and crowdions which occupy adjacent $\{110\}$ planes in an extended, three-dimensional arrangement. Further, our study suggests that even if self-interstitial clusters appear as dislocation loops, they would nucleate with a Burgers vector of $b = a/2\langle 111 \rangle$ rather than nucleating with $a/2\langle 110 \rangle$ and subsequently transforming to a perfect loop through a shear transformation as originally suggested by Bullough and Perrin [23].

3.2.2. Mobility of self-interstitials and self-interstitial clusters

Molecular-dynamics simulations of self-interstitial migration were performed over the temperature range of 100 $K \leq T \leq 1000$ K. Visualization of the simulation results led to the observation that self-interstitial migration in α-iron involves multiple mechanisms. Using the migration path observed in molecular-dynamics simulations with $T = 250$ K as a guide, molecular-statics simulations along the migration-path coordinate were performed to obtain a more quantitative picture of the barriers for the observed mechanisms. Fig. 12 shows a semi-quantitative picture of the two migration mechanisms and the magnitude of the energy barriers involved.

Based on our calculations, we conclude that self-interstitial migration in α-iron involves two mechanisms. One

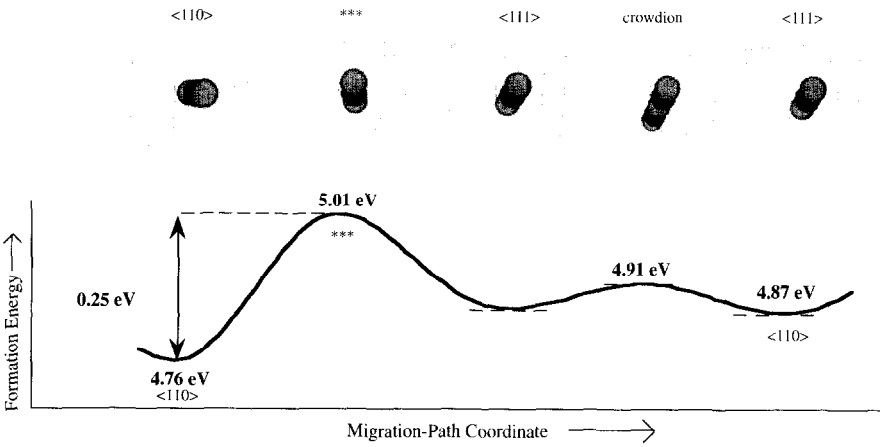

Fig. 12. Energetics of self-interstitial migration as a function of the migration-path coordinate. The self-interstitial configurations shown were obtained from molecular-dynamics simulation at $T = 250$ K and were relaxed fully for constructing this semi-quantitative plot.

mechanism involves rotation from the ⟨110⟩ to a ⟨111⟩-oriented dumbbell and the other is a translation of the dumbbell along the ⟨111⟩ direction. Once the self-interstitial has rotated into the ⟨111⟩ split-dumbbell configuration, it can make one or more translational jumps along ⟨111⟩ before rotating back to the lowest-energy ⟨110⟩ split-dumbbell configuration. The ⟨111⟩ translation has a very low energy barrier of 0.04 eV, i.e., it is practically an athermal migration process, while the rotation from ⟨110⟩ to a ⟨111⟩ dumbbell has an energy barrier of approximately 0.25 eV. The rotation from the ⟨111⟩ to ⟨110⟩ split-interstitial dumbbell configuration has an energy barrier of 0.14 eV.

The nature of the energy barriers for translation and rotation has profound effects on the kinetics of self-interstitial migration. Self-interstitials created as ⟨111⟩ dumbbells would be expected to migrate even at very low temperatures by translation until annihilation or rotation into a ⟨110⟩ configuration. Self-interstitials created as ⟨110⟩ dumbbells would be stable at low temperatures and require thermal activation to rotate to the ⟨111⟩ configuration and become mobile by translation in the ⟨111⟩ direction until the self-interstitial either annihilates with a vacancy-type defect, clusters with other self-interstitial defects, or rotates back into the ⟨110⟩ configuration.

Molecular-dynamics simulations of self-interstitial cluster migration were performed over the temperature range of $100 \leq T \leq 1000$ K for SIA cluster sizes ranging from $N = 2$ to 12. Visualization of the simulation results led to the observation that self-interstitial cluster migration in α-iron occurs by a single mechanism involving the collective ⟨111⟩ translations along the ⟨111⟩ orientation direction of the dumbbells and/or crowdions in the cluster by the 'local' disassociation and reassociation of self-interstitials to the cluster in an amoeba-like fashion. Complete disassociation of a self-interstitial from a cluster was not observed nor is it expected due to the high binding energies.

It is notable that self-interstitial clusters are capable of traveling large distances along the ⟨111⟩ orientation direction and that the migration is highly anisotropic. Although further simulations are required to provide a quantitative determination of the temperature dependence of self-interstitial cluster migration, we can conclude that the migration energy of small interstitial clusters is nearly the same as that of the single self-interstitial, $E^{M} \cong 0.1$ eV. This migration energy is much smaller than the binding energy of the clusters. The potential for these gliding clusters to be trapped by other clusters or point defects also needs further investigation. There is evidence in some of the long-running cascade simulations that these clusters can be very effectively trapped [4].

4. Summary

Molecular dynamics (MD) simulations of displacement cascades have been completed for energies up to 40 keV using a modified version of the embedded-atom interatomic potential developed for iron by Finnis and Sinclair. Although the results of these simulations are generally consistent with those obtained at lower energies, two notable exceptions were observed. The first is that extensive subcascade formation at 40 keV leads to a higher defect survival fraction than would be predicted by an extrapolation of the results obtained for energies up to 20 keV. The ratio of stable defects produced by the MD simulations to that calculated using the standard NRT model is a smoothly decreasing function up to 20 keV, but subcascade formation leads to an increase in this ratio at higher energies. The value of this ratio at 40 keV is about the same as at 10

keV. It was interesting to note that the sublinear dependence of stable defect formation on the MD cascade energy appeared to increase to ~ 1.0 at the highest energies. Thus, it may be that the linear energy dependence predicted by the NRT model will be observed in the regime of fully developed subcascades. In addition, the potential for a significant level of in-cascade vacancy clustering was observed. Previous cascade studies employing this potential have observed extensive interstitial clustering, but little evidence of vacancy clustering. The results reported here suggest that this may be due to an overly strict criterion for clustering. When the spatial arrangement of the residual vacancies was examined, evidence of vacancy–vacancy correlation was observed at the second and fourth nearest neighbor distances. Since vacancies are essentially immobile over the time scale accessible by the MD method, these correlated vacancies may represent nascent clusters.

A comprehensive atomistic study of the structure, and the formation and migration energetics of the self-interstitial and small ($N = 2$ to 19) self-interstitial clusters in α-iron has been completed. This research has revealed that the stable cluster configurations are highly complex, three-dimensional structures consisting of ⟨111⟩ oriented dumbbells and/or crowdions which occupy adjacent {110} planes. MD simulations over a wide temperature range have revealed that single interstitial migration is a two-step process involving rotations out of and into the ground-state ⟨110⟩ dumbbell configuration and translation of ⟨111⟩ dumbbells through the crowdion saddle-point configuration. Self-interstitial clusters are quite mobile and they migrate in a highly anisotropic, one-dimensional manner along their ⟨111⟩ orientation.

When taken together with the previous work, these MD and MC simulations provide a reasonably complete description of primary defect formation and point defect behavior in iron. However, it should be pointed out that the conclusions reached are subject to details implicit in the interatomic potential used for the simulations. In this case, it is perhaps safer to say that we have well characterized an iron-like material that one could call Finnis–Sinclairium. For example, the embedded-atom type potentials are isotropic and the influence of directional, d-orbital bonding could be significant in a transition metal such as iron. Since the formation energies for the alternate types of interstitials are similar, directional bonding could influence the relative stability of the different possible orientations. The very low interstitial cluster migration energies could also be affected. Conversely, the results of the cascade simulations should be less sensitive to the fine details of the potential since primary defect formation is primarily controlled by events that occur at relatively high energies. The point defect survival and point defect clustering fractions derived from the MD results should provide reliable guidance for obtaining the parameters required in the kinetic models used to simulate radiation-induced microstructural evolution and mechanical property changes [25].

Acknowledgements

The authors would like to acknowledge the results obtained in collaboration with Dr D.J. Bacon, Dr A.F. Calder, Dr A.J.E. Foreman and Dr W.J. Phythian and helpful discussions with Dr G.E. Lucas, Dr D. Maroudas and Dr S.J. Zinkle. Research sponsored at Oak Ridge National Laboratory by the Division of Materials Sciences and the Office of Fusion Energy, US Department of Energy and by the Office of Nuclear Regulatory Research, US Nuclear Regulatory Commission under inter-agency agreement DOE 1886-8109-8L with the US Department of Energy under contract DE-AC05-96OR22464 with Lockheed Martin Energy Research Corp. and at the University of California by the Office of Nuclear Regulatory Research, US Nuclear Regulatory Commission.

References

[1] J.B. Gibson, A.N. Goland, M. Milgram, G.H. Vineyard, Phys. Rev. 120 (1960) 1229.
[2] R.E. Stoller, JOM 48 (1996) 23.
[3] W.J. Phythian, R.E. Stoller, A.F. Calder, A.J.E. Foreman, D.J. Bacon, J. Nucl. Mater. 223 (1995) 245.
[4] R.E. Stoller, Molecular Dynamics Simulations of High Energy Cascades in Iron, Microstructure of Irradiated Materials (Materials Research Society, Pittsburgh, PA, 1995) pp. 21–26.
[5] A.F. Calder, D.J. Bacon, J. Nucl. Mater. 207 (1993) 25.
[6] R.E. Stoller, J. Nucl. Mater. 233–237 (1996) 999.
[7] D.J. Bacon, A.F. Calder, J.M. Harder, S.J. Wooding, J. Nucl. Mater. 205 (1993) 52.
[8] A.J.E. Foreman, C.A. English, W.J. Phythian, Philos. Mag. A66 (1992) 671.
[9] T. Diaz de la Rubia, M.W. Guinan, Mater. Sci. Forum 97–99 (1992) 23.
[10] R.S. Averback, J. Nucl. Mater. 216 (1994) 49.
[11] D.J. Bacon, A.F. Calder, F. Gao, V.G. Kapinos, S.J. Wooding, Nucl. Instrum. Meth. B102 (1995) 37.
[12] J.B. Adams, A. Rockett, J. Kieffer, W. Xu, M. Nomura, K.A. Kilian, D.F. Richards, R. Ramprasand, J. Nucl. Mater. 216 (1994) 265.
[13] M.W. Finnis, J.E. Sinclair, Philos. Mag. A50 (1984) 45; erratum, Philos. Mag. A53 (1986) 161.
[14] B.D. Wirth, G.R. Odette, D. Maroudas, G.E. Lucas, J. Nucl. Mater. 244 (1997) 185.
[15] J.M. Harder, D.J. Bacon, Philos. Mag. A58 (1988) 165.
[16] M.W. Finnis, MOLDY6: A Molecular Dynamics Program for Simulation of Pure Metals, AERE R-13182, UKAEA Harwell Laboratory, 1988.
[17] F. Gao, D.J. Bacon, P.E.J. Flewitt, T.A. Lewis, J. Nucl. Mater. 249 (1997) 77.
[18] D.J. Bacon, T. Diaz de la Rubia, J. Nucl. Mater. 216 (1994) 275.

[19] M.J. Norgett, M.T. Robinson, I.M. Torrens, Nucl. Eng. Des. 33 (1975) 50.
[20] ASTM E693, Standard Practice for Characterizing Neutron Exposures in Ferritic Steels in Terms of Displacements per Atom (dpa), Annual Book of ASTM Standards, Vol. 12.02 (American Society of Testing and Materials, Philadelphia, PA).
[21] ASTM E521, Standard Practice for Neutron Radiation Damage Simulation by Charged-Particle Irradiation, Annual Book of ASTM Standards, Vol. 12.02 (American Society of Testing and Materials, Philadelphia, PA).
[22] D. Maroudas, R.A. Brown, Phys. Rev. B47 (1993) 15562.
[23] R. Bullough, R.C. Perrin, Proc. R. Soc. London A305 (1968) 541.
[24] P. Ehrhart, K.H. Robrock, H.R. Schober, Physics of Radiation Effects in Crystals, MPCMS, Vol. 13 (North-Holland, Amsterdam, 1986).
[25] R.E. Stoller, L.R. Greenwood, 'Influence of subcascade formation on displacement damage at high PKA energies', presented at the Symp. on Materials for Spallation Neutron Sources, 1997 Annual Meeting of TMS, Orlando, FL, Feb. 9–13, 1997, submitted for publication to TMS.